The Aeronautical Journal (2026), 1–19
doi:10.1017/aer.2026.10231

RESEARCH ARTICLE

Numerical analysis and reduced-order modelling of a variable area mixer

Maura Ponti[1], Karel Van den Borre[1,2], Giuseppe Mattia Bruno[1] and Bayindir Huseyin Saracoglu[1]

[1]Turbomachinery and Propulsion, Von Karman Institute For Fluid Dynamics, Sint Genesius Rode, Belgium
[2]BRITE Research Group, Vrije Universiteit Brussel, Ixelles, Belgium
Corresponding author: Karel Van den Borre; Email: karel.vandenborre@vki.ac.be

Received: 28 February 2026 UTC; **Revised:** 3 August 2026 UTC; **Accepted:** 4 August 2026 UTC

Keywords: computational fluid dynamics; reduced order modelling; variable area bypass injector; variable cycle engine

Abstract

Variable cycle engines (VCEs) are an emerging class of propulsion systems designed to adapt their thermodynamic cycle to changing flight conditions, enabling both high efficiency at subsonic speeds and high specific thrust at supersonic speeds. A key enabler of this flexibility is the variable area bypass injector (VABI), which controls the bypass-to-core mass flow ratio and influences overall engine performance. Despite its importance, the aerodynamic behaviour of VABIs, particularly in terms of bypass flow entrainment and associated pressure losses, has received limited attention in the literature. This paper focuses on the rear VABI, a component analogous to the mixer in conventional turbofans but equipped with an area-regulating mechanism to vary the bypass cross-sectional area. The study consists of two parts: first, high-fidelity three-dimensional computational fluid dynamics (CFD) simulations are performed to characterise the rear VABI. A range of operating conditions and area regulator positions have been assessed, emphasising the total pressure losses and bypass flow entrainment. Secondly, the CFD results have been processed into a non-dimensional performance database used to develop a reduced-order VABI model. This VABI model has been integrated into a notional three-stream VCE configuration to demonstrate its applicability in system-level analyses. The proposed methodology bridges detailed CFD simulations and a computationally efficient representation, enabling accurate modelling of VABI behaviour within broader engine design frameworks.

Nomenclature

BPR	bypass ratio
CFD	computational fluid dynamics
IV	iteration variable
RANS	Reynold-averaged Navier-Stokes
VABI	variable area bypass injector
VCE	variable cycle engine
A	area
A_b/A_c	bypass to core area ratio
D	diameter
p	static pressure
R	specific gas constant
T	temperature
$\Delta\mathcal{M}^{rel}$	relative momentum difference
β	mathematical map parameter

This paper was presented at the 27th Conference of the International Society for Air Breathing Engines (ISABE) which was held on 20–25 September 2026 in Mumbai, India.

© The Author(s), 2026. Published by Cambridge University Press on behalf of Royal Aeronautical Society. This is an Open Access article, distributed under the terms of the Creative Commons Attribution licence (https://creativecommons.org/licenses/by/4.0/), which permits unrestricted re-use, distribution and reproduction, provided the original article is properly cited.

Downloaded from https://www.cambridge.org/core. 17 Nov 2026 at 02:24:13, subject to the Cambridge Core terms of use.

ρ	density
σ	pressure loss coefficient
η	thermodynamic efficiency
x_{b}	bypass
x_{c}	Core
x_{corr}	corrected quantity
x_{ref}	reference condition (ISA)
x_{t}	total conditions
x_{mp}	mixing plane
$\dot{x}$	mass or volumetric flow rate

1.0 Introduction

Coaxial mixers are used in multiple engineering applications. A first broad category is ejector systems, in which a high-pressure central flow entrains a secondary flow. As these systems have no moving parts, they have a low operational cost. They can be used to improve refrigeration cycle efficiency [1], recover low-grade waste heat in propulsion systems [2] and for other industrial applications [3, 4]. Furthermore, mixers are a core component of mixed-flow turbofan engine architectures, where their pressure recovery and mixing efficiency significantly impact the overall engine performance [5]. Among the turbofan mixers, the most common are the fixed-geometry coaxial-lobed mixers. Their performance has been extensively studied both numerically and experimentally. Fejer et al. conducted experimental and analytical investigations of confined coaxial mixing of isoenergetic air streams [6], deriving new analytical expressions for eddy viscosity and turbulent diffusion coefficient valid in regions where existing formulations become indeterminate. Hu et al. [7] conducted an experimental study of a canonical low-speed lobed nozzle, used as a validation case in subsequent numerical studies by Cooper et al. [8], that proved the predictability of the turbulence models in modelling a lobed jet mixing flow.

For large-scale system-of-systems simulations, computational efficiency is a critical concern. As a result, low-fidelity models are often employed. Although these models lack the accuracy of experimental data or high-fidelity computational fluid dynamics (CFD) simulations, they can provide sufficiently reliable results at a significantly reduced computational cost. In aircraft engine simulations, researchers frequently use zero-dimensional mixer models based on control-volume formulations [4, 9]. While computationally efficient, these models require empirical knowledge of component efficiencies, which is often unavailable. As a compromise, one-dimensional modelling approaches have been proposed [10, 11], which strike a balance between the computational cost, accuracy and a priori required empirical knowledge. Variable cycle engines (VCEs) are a new class of propulsion systems capable of altering their thermodynamic cycle to match changing flight conditions. This adaptability allows them to operate efficiently during subsonic cruise and deliver a high specific thrust during supersonic cruise by raising and lowering the bypass ratio, respectively. VCEs achieve this flexibility through variable-geometry components that regulate airflow throughout the engine, such as variable area bypass injector (VABI), Variable Stator Vanes, compressor inlet guide vanes (IGVs), and variable-area exhaust nozzles. The ability to change the geometry of these components in situ enhances the system's operational flexibility, thereby improving efficiency in off-design conditions [12, 13].

The performance of VABIs in terms of total pressure losses and entrained bypass flows is critical for assessing the feasibility of these new engine architectures, yet it remains sparsely addressed in the literature. This work investigates the rear VABI, a component that operates analogously to a mixer in conventional turbofans, but can alter the bypass-to-core area ratio via an area regulator. To characterise its behaviour, a parametric CFD study has been conducted on a geometry adapted from Liu et al. [14]. From the CFD simulations campaign, reduced performance maps have been obtained, and the robustness of this parameter reduction is being evaluated under a range of realistic off-design conditions. These maps are then embedded in a reduced-order VABI component within a notional three-stream VCE architecture. This methodology aims to bridge high-fidelity three-dimensional CFD insights with a computationally efficient zero-dimensional representation suitable for system-level design studies.

Downloaded from https://www.cambridge.org/core. 17 Nov 2026 at 02:24:13, subject to the Cambridge Core terms of use.

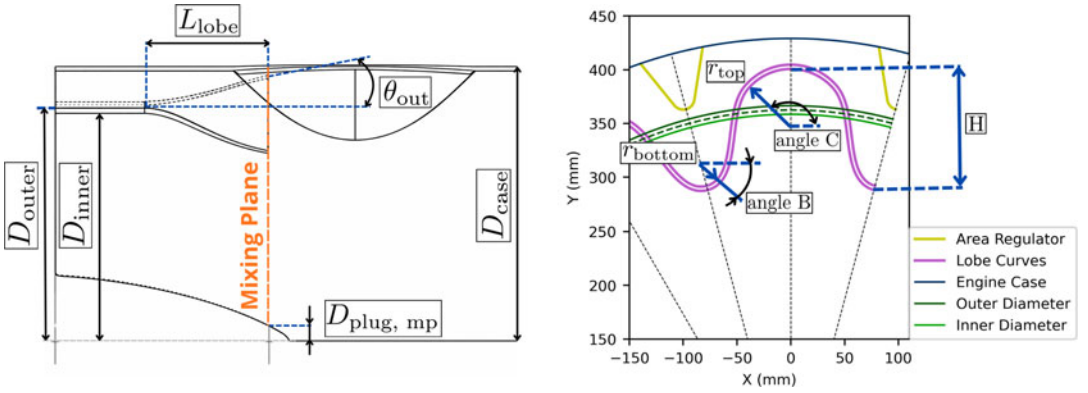
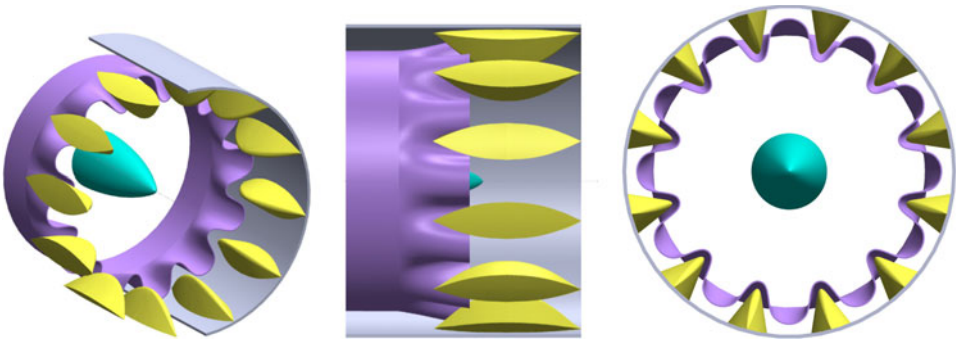


Figure 1. *Lateral view of the geometry (left) and view of the lobed profile at the mixing plane (right).*



(a) Perspective view (b) Lateral view (c) Front view

Figure 2. *3D view of the Rear-VABI geometry.*

2.0 CFD study of the VABI

This section describes the Reynolds-averaged Navier-Stokes (RANS)-based CFD simulations used to generate performance maps and to validate the parameter reduction approach. RANS has been successfully applied to reproduce the key flow features of similar mixing systems, including lobed jets [8], ejector systems [15] and jet-engine mixers [16]. These studies indicate that RANS provides sufficient accuracy for the present application, while avoiding the significant computational cost penalty associated with alternatives such as Large Eddy Simulation or Detached Eddy Simulation.

2.1 Geometry and meshing

The configuration object of this study is a 12-lobe mixer (see Figures 1 and 2) equipped with an area regulator that enables adjustment of the bypass-to-core area ratio at the mixing plane. This area regulator consists of 12 bumps that can move axially and slot into the mixer's lobes. As such, the area regulator can only vary the bypass area, altering the total flow area at the mixing plane.

This geometry concept is proposed by Liu et al. [14]. Its advantages are that the moving parts are only exposed to the cold bypass flow and that the mechanical actuator structure is simple. Moreover, the characteristic lobe geometry enhances mixing by generating large-scale vortices at the trailing edge of the lobes. However, this shape increases the wetted surface area, leading to higher total pressure losses [17].

The geometry of a single lobe is defined through a set of characteristic parameters commonly adopted in previous studies [18, 19]. These include the lobe height (H), the number of lobes (N) and the area ratio between bypass and core streams at the mixing plane (A_b/A_c). The extent of the lobes in the axial direction is defined by (L_{lobe}), while the radial extent is defined by the penetration angle (θ).

Downloaded from https://www.cambridge.org/core. 17 Nov 2026 at 02:24:13, subject to the Cambridge Core terms of use.

Table 1. *Inputs of the geometry generation tool*

Parameter	Value
$A_{b,\,\mathrm{mp}}(\mathrm{mm}^2)$	0.133×10^6
$A_{c,\,\mathrm{mp}}$ (mm^2)	0.398×10^6
D_{inner} (mm)	697
$D_{\mathrm{plug,\ mp}}$ (mm)	50
θ_{out} (°)	13
r_{top} (mm)	55
r_{bottom} (mm)	20
angle B (°)	−60
angle C (°)	140
Thickness (mm)	4
L_{lobe} (mm)	200

Table 2. *Outputs of the geometry generation tool*

Parameter	Value
H(mm)	109
D_{case} (mm)	835
D_{outer} (mm)	713
$A_{c,\,\mathrm{inlet}}$ (mm^2)	0.153×10^6
$A_{b,\,\mathrm{inlet}}$ (mm^2)	0.354×10^6

Each half-lobe is modelled using two circular arcs describing the bottom and top parts of the profile, of radii r_{bottom} and r_{top}, connected by a Bézier curve to ensure tangency and geometric continuity. All geometric quantities are expressed as functions of prescribed design parameters, with the lobe height being a free variable. This parameter is computed iteratively to obtain a target area ratio between core and bypass areas at the mixing plane. This parametrisation allows the lobe geometry to be uniquely determined from a minimal set of input parameters and enables rapid generation of geometries that are consistent with prescribed flow-area constraints.

The area regulator profile at the mixing plane is fixed and is included in the bypass area calculation to ensure consistency with the imposed area ratio. It is defined by a circular arc of radius 21 mm and an angle of 18 degrees. This arc is then connected to the engine case by a straight line inclined at 81 degrees to the horizontal. The area regulator extends over an axial length of 400 mm. The lobes are integrated within a coaxial duct configuration defined by an inner diameter D_{inner} and an outer diameter D_{outer}. The difference between these diameters determines the local lobe thickness, which varies along the axial direction, from 8 mm at the duct junction to 4 mm at the trailing edge of the lobes. A central plug is included and is characterised by its diameter at the mixing plane $D_{\mathrm{plug,\,mp}}$, and at the inlet section of 200 mm. The total axial length of the mixing chamber, measured from the inlet to the outlet plane, is 1,400 mm.

The values of the geometrical parameters are summarised in Table 1, while the corresponding geometric quantities computed by the geometry-generation tool are listed in Table 2. The geometric meaning of these parameters is illustrated in Figure 1.

Given the geometric periodicity, a domain containing a single lobe was selected for the CFD study, with periodic boundary conditions applied on the lateral planes. A representation of the domain, containing a single 30-degree sector, is shown in Figure 3.

Downloaded from https://www.cambridge.org/core. 17 Nov 2026 at 02:24:13, subject to the Cambridge Core terms of use.

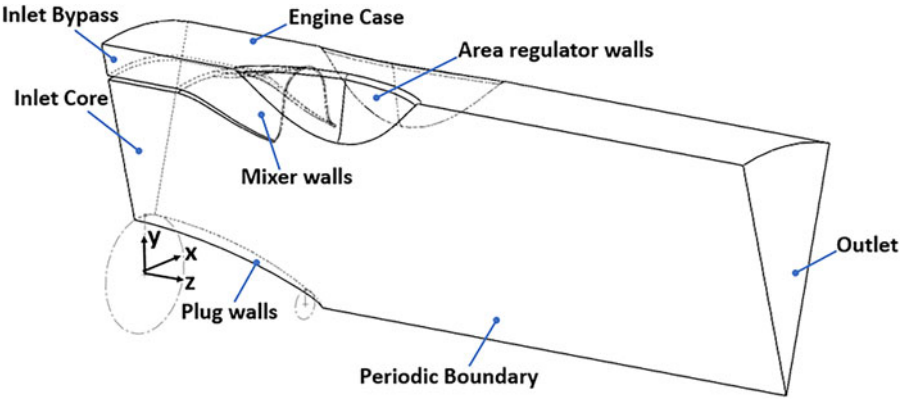


Figure 3. *Computational domain for the numerical simulations.*

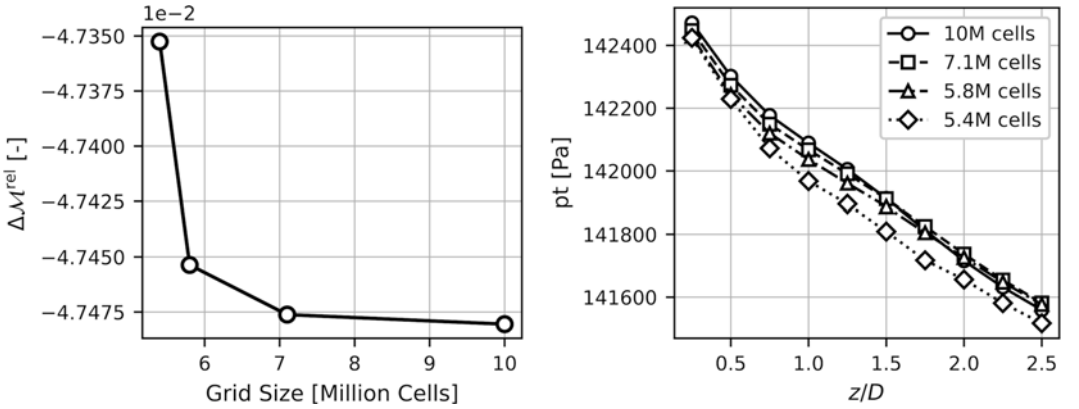


Figure 4. *Mesh convergence trend of the relative momentum difference (left) and total pressure at different axial positions (right).*

The computational domain is discretised using an unstructured mesh with localised volume refinement downstream of the lobe. The boundary layer first cell height is imposed equal to 2×10^{-6}m to maintain a wall y + value below 1, thereby fully resolving the viscous sublayer. Twenty-seven prismatic layers are used, with a growth rate of 1.25, ending with a total inflation layer thickness of approximately 1.7 mm, which smoothly transitions to the core mesh.

A mesh independence study was performed to determine the minimum grid resolution, which provides mesh-independent results at an acceptable computational cost. Four meshes were generated by scaling an initial mesh using cell length multipliers of 2, 1, 0.7 and 0.5. The reference mesh sizes were 0.015 m for the global mesh and 0.009 m and 0.008 m for two local refinement regions. Mesh convergence was assessed in terms of the axial total pressure evolution and the relative momentum difference between inlets and outlets, as defined by Equations (1) and (2). The results of the mesh convergence study are shown in Figure 4. Based on these results, the mesh with a multiplier of 0.7 (7.1 million cells) provides a satisfactory trade-off between accuracy and cell count. The final mesh is depicted in Figure 5.

$$\Delta\mathcal{M}^{\text{rel}} = \frac{\mathcal{M}_{\text{in}} - \mathcal{M}_{\text{out}}}{\mathcal{M}_{\text{in}}} \tag{1}$$

$$\mathcal{M} = \int_A \rho v^2 \, \mathrm{d}A + \int_A p \, \mathrm{d}A \tag{2}$$

Downloaded from https://www.cambridge.org/core. 17 Nov 2026 at 02:24:13, subject to the Cambridge Core terms of use.

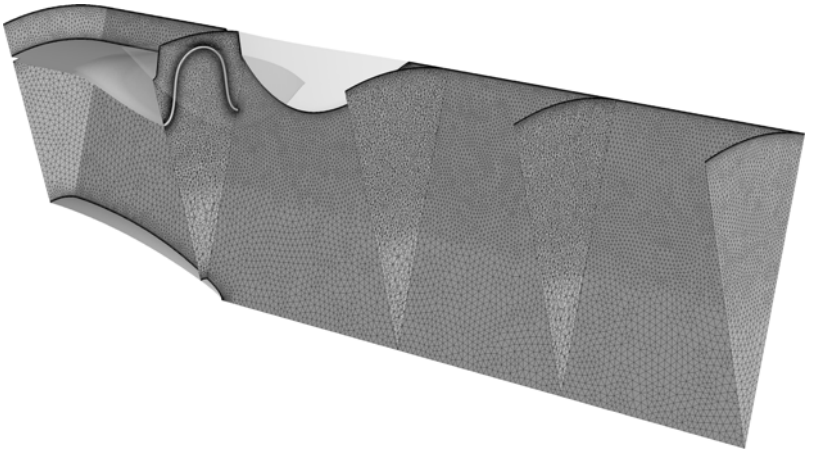


Figure 5. *Mesh selected during the mesh convergence study.*

2.2 Numerical setup and boundary conditions

The simulations are performed using the ANSYS Fluent 2024R2 pressure-based solver, which is suitable for simulating flows in the compressible subsonic regime experienced in this study [20, 21]. The working fluid is treated as an ideal gas with properties corresponding to air. The contribution of combustion products to the core-stream composition is neglected. This approximation primarily influences thermophysical properties, including the specific heat and the specific gas constant. The resulting impact on the VABI performance is expected to be minor and is therefore omitted from the present analysis.

Convective terms are discretised using a second-order upwind scheme. Pressure–velocity coupling is achieved using the coupled algorithm. The energy equation is enabled to account for compressibility effects, which become significant at the flow velocities encountered in the VABI, reaching up to Mach 0.5. Density is updated iteratively using the ideal gas law. The realisable k-ϵ model is selected as the turbulence model, which, as will be demonstrated in the validation (Section 2.3), has shown the closest match to experimental results for similar turbulent mixing cases. Turbulence levels at the inlets are estimated at 3% for the fan flow and 5% for the turbine flow. The boundary conditions consist of total pressure and temperature at the inlets, static pressure at the outlet and periodic boundary conditions on the sector faces to exploit the geometry's periodicity. All walls have the no-slip condition applied.

2.3 Validation of lobed mixers

To validate the RANS approach, a comparison was performed between the numerical results and the experimental investigation of Hu et al. [7], which examines the flow field of an air jet discharged into the ambient environment through a lobed nozzle. Three different turbulence models have been assessed: k- ε realisable, $k-\omega$ shear strain turbulence (SST) model and Spalart–Allmaras.

Quantitative comparisons between numerical predictions and DP-SPIV measurements show good overall agreement for peak streamwise (ω_z) and azimuthal ($\omega_{\text{azimuthal}}$) vorticity (Figure 6). For azimuthal vorticity, all models fall within experimental uncertainty beyond $Z/D = 2$, whereas upstream the Spalart–Allmaras and k–ω SST models overpredict by up to 118%, compared to about 42% for the realisable k–ε model. A similar trend is observed for streamwise vorticity: agreement is reached beyond $Z/D = 1.75$, while closer to the nozzle deviations increase to 111% for the Spalart–Allmaras and k–ω SST models, but remain within 14% for the realisable k–ε model. Overall, the realisable k–ε model shows the best agreement, indicating that a RANS approach with a two-equation turbulence model captures the dominant flow features.

Downloaded from https://www.cambridge.org/core. 17 Nov 2026 at 02:24:13, subject to the Cambridge Core terms of use.

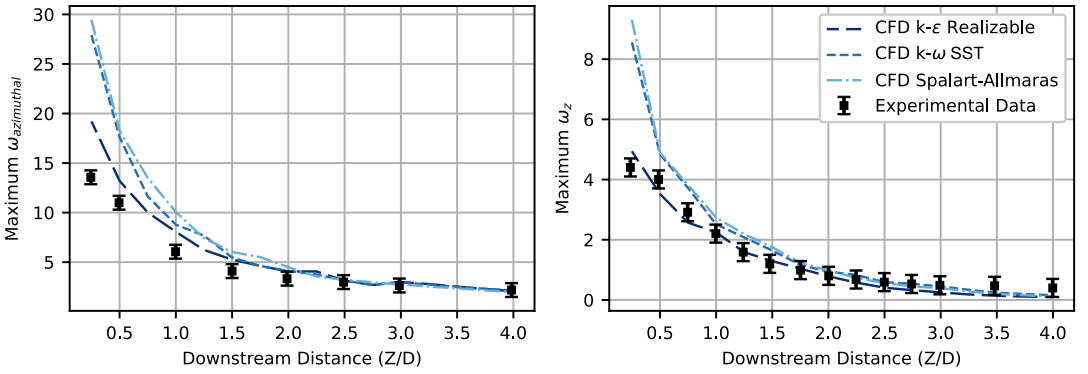


Figure 6. *Validation of the model: decay along the streamwise direction of the maximum streamwise and azimuthal vorticity.*

Table 3. *Parameter values for the test matrix*

Parameter	Value(s)
$p_{t,c}$ (Pa)	144013
$p_{t,b}/p_{t,c}$	0.94–1.20
$p_{out}/p_{t,c}$	0.86–0.98
$T_{t,c}$ (K)	935
$T_{t,b}/T_{t,c}$	0.3983
A_b/A_c	0.255, 0.283, 0.335, 0.376

2.4 Results

To generate the performance map for the VABI, numerical simulations are performed with boundary conditions imposed to replicate the thermodynamic states encountered during typical engine operation. The operability of the VABI was investigated over a range of area ratios A_b/A_c between 0.255 and 0.376, corresponding to different axial positions of the area regulator. The simulations were performed for inlet total pressure ratios $p_{t,b}/p_{t,c}$ varying from 0.94 to 1.20 and for static outlet to total core inlet pressure ratios spanning from 0.86 to 0.98. The boundary conditions employed in this study are summarised in Table 3.

Figure 7 illustrates the development of the flow along the axial direction for the case with $A_b/A_c = 0.335$, $p_{t,b}/p_{t,c} = 1.00$ and $p_{out}/p_{t,c} = 0.86$. The flow evolution is visualised along a series of cross-sectional planes located at different axial positions downstream of the mixing plane. The plane locations are normalised between the mixing plane ($z/L = 0$) and the mixer exit ($z/L = 1$). This figure shows how the vortices generated by the lobes mix the slower bypass flow into the faster core flow.

Figure 8 displays the contours of Mach number, streamwise vorticity and total temperature for four operating conditions. The operating conditions are summarised in Table 4, and the streamwise vorticity is defined as:

$$\omega_z = \left(\frac{\partial v}{\partial x} - \frac{\partial u}{\partial y} \right) \tag{3}$$

The vorticity field, presented in Figure 8, highlights the development of the shear layer and the formation of large-scale vortical structures downstream of the mixer trailing edge. The lobed shape of the mixer induces strong rotational motion, promoting momentum exchange between the core and bypass streams and enhancing mixing, leading to a more uniform distribution of thermodynamic quantities at the outlet. The vorticity colour scale ranges from $-3,000$ to $3,000$, where positive values (red) denote

Downloaded from https://www.cambridge.org/core. 17 Nov 2026 at 02:24:13, subject to the Cambridge Core terms of use.

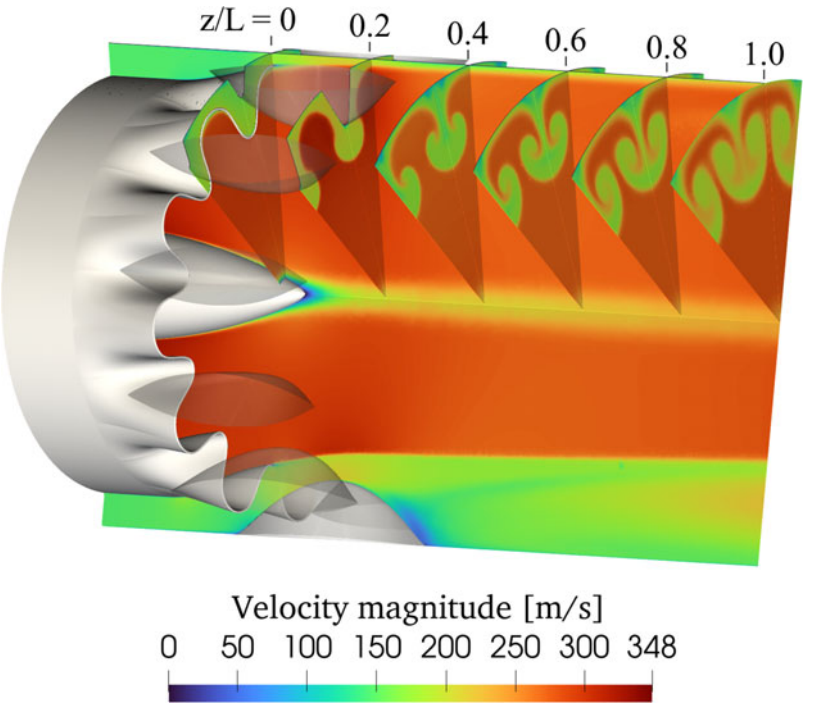


Figure 7. *Axial evolution of the flow field, visualised on multiple cross-sectional planes at increasing downstream locations.*

counter-clockwise rotating structures and negative values (blue) indicate clockwise rotation, as viewed in the downstream direction.

A comparison between cases a and c shows that increasing the outlet static pressure primarily reduces the momentum of both streams, resulting in lower Mach numbers and lower streamwise vorticity levels, while the vortical structure shape remains unchanged. In contrast, increasing the inlet total pressure ratio (case b) increases the mass flow rate of the bypass stream with respect to the core stream, leading to higher local Mach numbers but reduced mixing efficiency, as evidenced by a less uniform total temperature distribution at the outlet compared to the reference case. Finally, reducing the bypass area (case d) significantly alters the spatial development of the vortical structures, thereby modifying the downstream evolution of the flow field and associated thermodynamic quantities.

Figure 9 displays the static pressure distribution for case a. A common assumption in the literature for modelling the rear VABI, or a conventional constant-area duct mixer, is that the two streams have equal static pressure at the mixing plane. This hypothesis corresponds to the ideal case, where all flow is axial, and is used in zero-dimensional mixer models, as it provides a closure equation for determining the bypass flow rate. However, this assumption may not hold for a highly three-dimensional flow, such as that which develops in a lobed mixer. Indeed, the vortices generated by the lobes lead to curvature in the streamlines, which generate a pressure gradient in the direction normal to the streamline towards the local radius of curvature, though the streamline curvature equation:

$$\frac{\partial p}{\partial n} = \rho \frac{v^2}{R} \tag{4}$$

with $\partial p/\partial n$ the pressure gradient normal to the streamline in the direction of the local curvature, v the velocity and R the radius of the streamline curvature. The results, as seen in Figure 9, show that static-pressure equilibrium is indeed not achieved immediately at the mixer trailing edge, with the presence of high-pressure zones near the walls. Furthermore, two low-pressure zones remain at the centres of the

Downloaded from https://www.cambridge.org/core. 17 Nov 2026 at 02:24:13, subject to the Cambridge Core terms of use.

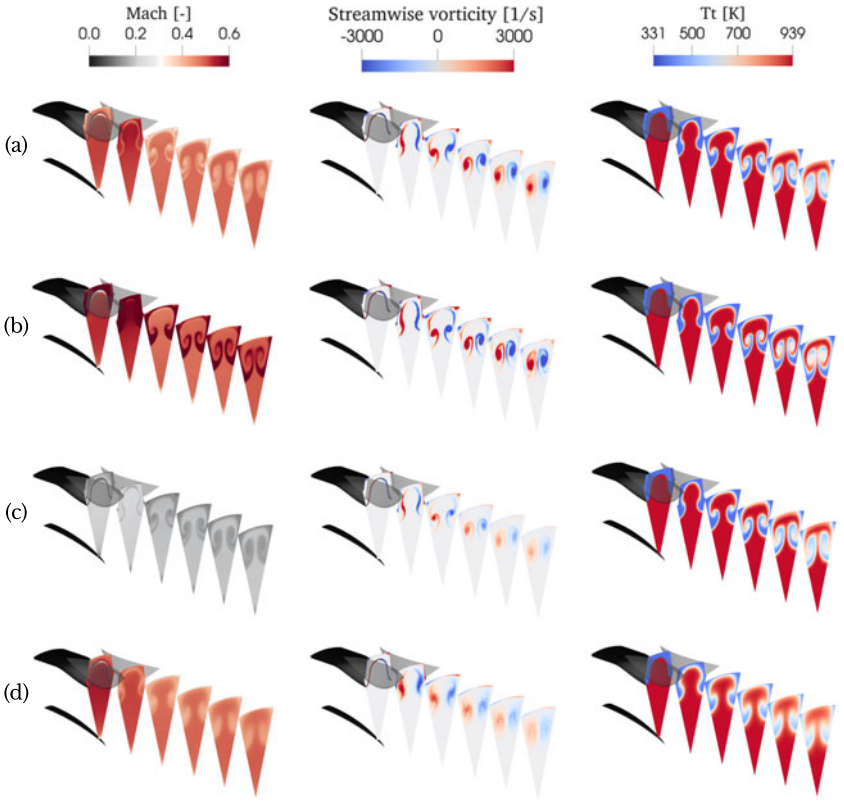


Figure 8. *Contours of Mach, ω_z and total temperature fields for the cases defined in Table 4.*

Table 4. *Boundary conditions of the cases depicted in Figure 8*

Case	$p_{t,b}/p_{t,c}$	A_b/A_c	$p_{out}/p_{t,c}$
a	1.00	0.335	0.86
b	1.20	0.335	0.86
c	1.00	0.335	0.97
d	1.00	0.255	0.86

vortices generated by the lobes, which don't dissipate before reaching the mixer exit, where a uniform static pressure balance is imposed. This observation is consistent with the findings of Huang et al. [17], which state that static-pressure equivalence occurs only when the velocity component perpendicular to the axial direction becomes negligible. In the present configuration, the mixer geometry is specifically designed to promote radial transport, and a static-pressure mismatch between the streams is expected. Finally, observing Figure 9, a sudden static pressure drop can be noticed at $z/L = 0.2$. This drop occurs in correspondence with the area regulator, whose presence reduces the flow passage area. As a result, the flow accelerates, leading to a static pressure drop.

3.0 Reduced order mixer model

A VABI performance map must characterise the component across its operating envelope: for any given set of input parameters, a unique operating point is identified, and the corresponding performance

Downloaded from https://www.cambridge.org/core. 17 Nov 2026 at 02:24:13, subject to the Cambridge Core terms of use.

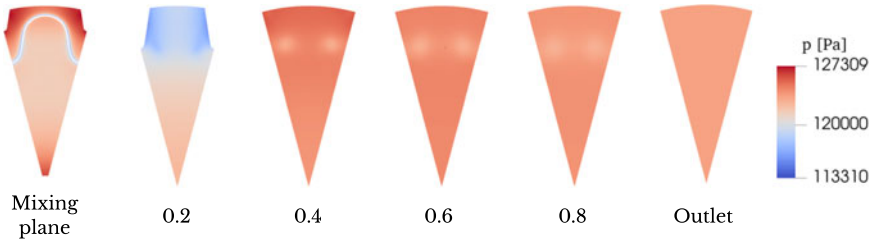


Figure 9. *Static pressure distribution for case a in Table 4.*

metrics can be retrieved. The rear-VABI has two thermodynamic inlets and one thermodynamic outlet. The following six parameters fully describe the thermodynamic state at both inlets, the position of the area regulator and the mass flow rate through the VABI:

$$\frac{p_{\mathrm{t,b}}}{p_{\mathrm{t,c}}}, \quad \frac{p_{\mathrm{out}}}{p_{\mathrm{t,c}}}, \quad \frac{T_{t,b}}{T_{t,c}}, \quad p_{\mathrm{t,c}}, \quad T_{t,c}, \quad \frac{A_{\mathrm{b}}}{A_{\mathrm{c}}} \tag{5}$$

The total thermodynamic state in the core inlet is directly imposed by p_c and T_c. Combined with $p_{\mathrm{t,b}}/p_{\mathrm{t,c}}$ and $T_{t,b}/T_{t,c}$, also the bypass inlet is completely defined. $A_{\mathrm{b}}/A_{\mathrm{c}}$ defines the setting of the area regulator, which would not be present in a conventional, fixed-geometry mixer. The mass flow rates are indirectly determined by $p_{\mathrm{exit}}/p_{\mathrm{t,c}}$, with a lower value of $p_{\mathrm{exit}}/p_{\mathrm{t,c}}$ leading to higher mass flow rates. For the performance map, it is beneficial to use $\dot{m}_c$ instead of $p_{\mathrm{out}}/p_{\mathrm{t,c}}$, as p_{out} is an output of a system-level component model and, as such, not directly accessible, unlike an inlet mass flow rate.

The performance of the VABI component can be described by a set of non-dimensional and reduced parameters (also called corrected parameters). By doing so, the VABI's performance collapses to a single value across different absolute input parameters, provided the corrected parameters are kept constant. This reduces the number of input parameters required to fully describe the VABI's state, lowering the map's dimensionality and the number of expensive, high-fidelity simulations needed to sample a given coverage. A similar procedure is employed to generate performance maps for compressors and turbines [9]. The following non-dimensional and corrected parameters are used to describe the performance map:

$$\frac{p_{\mathrm{t,b}}}{p_{\mathrm{t,c}}}, \quad \dot{m}_{\mathrm{corr},c}, \quad \frac{A_{\mathrm{b}}}{A_{\mathrm{c}}} \tag{6}$$

with the core-corrected core mass flow rate $\dot{m}_{\mathrm{corr},c}$ being defined as:

$$\dot{m}_{\mathrm{corr},c} = \frac{\dot{m}_c \sqrt{(T_{t,c}\, R)/(T_{t,ref}\, R_{ref})}}{p_{\mathrm{t,c}}/p_{t,ref}} \tag{7}$$

Having defined the input parameters for the map, the output parameters that characterise the component performance need to be selected. The performance of the rear-VABI is primarily assessed using two metrics: its flow regulation ability, and the pressure losses in the system [16, 22, 23]. Flow regulation capability is defined as the degree to which geometric variations of the VABI control the bypass mass flow fraction entering the component. Flow regulation capability can be quantified through quantities as the bypass ratio, defined as the ratio between bypass and core mass flow rates $\mathrm{BPR} = \dot{m}_b/\dot{m}_c$, or the absolute mass flow rates that enter the system. Given that the core mass flow rate is already used as an input for the map, the bypass mass flow rate is selected as the relevant performance parameter.

Total pressure loss characterises the aerodynamic efficiency of the component and the mixing process. Pressure losses in a mixing process arise from wall friction, flow separation, and entropy generation.

Downloaded from https://www.cambridge.org/core. 17 Nov 2026 at 02:24:13, subject to the Cambridge Core terms of use.

Table 5. *Test matrix for the sensitivity analysis of inlet total temperature ratio effects on rear-VABI performance*

$p_{t,b}/p_{t,c}$	$T_{t,b}/T_{t,c}$
0.98	0.370, 0.488
1.02	0.200, 0.370, 0.488, 0.600

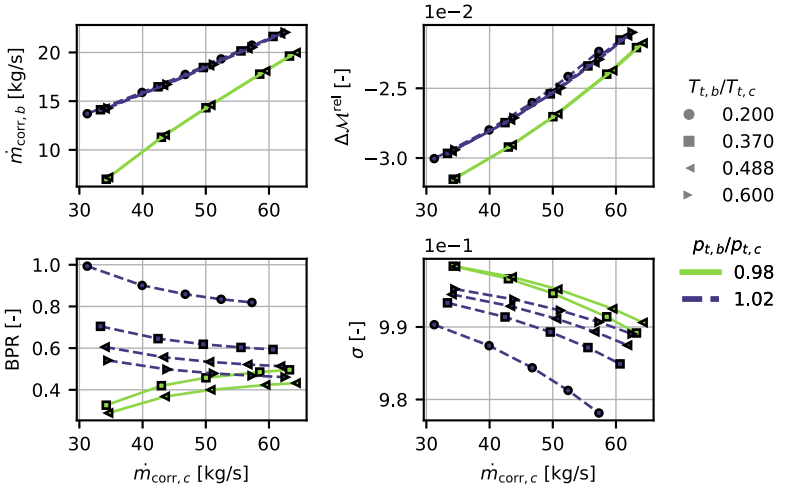


Figure 10. *Sensitivity of the performance parameters of interest to variations in the inlet total temperature ratio for two constant inlet total pressure ratios.*

A parameter generally used to quantify this loss is the total pressure loss coefficient, defined as:

$$\sigma = \frac{\frac{1}{m_{out}} \int p_{t,out}\, dm_{out}}{\frac{1}{m_{in}} \int p_{t,in}\, dm_{in}} \tag{8}$$

where the numerator represents the outlet mass flow-averaged total pressure $p_{t,out}$, while the denominator corresponds to the equivalent mass-flow-averaged inlet total pressure.

3.1 Choice of the outlet parameters and validation of the map

An assumption commonly used in the literature is to neglect the influence of the total temperature ratio on the performance parameters of the VABI, assuming the other non-dimensional parameters will have a stronger effect [22, 23]. To assess the validity of this assumption, additional simulations were conducted with varying inlet total temperature ratios while maintaining all other boundary conditions constant. The investigated operating points are summarised in Table 5. Two inlet total pressure ratios $p_{t,b}/p_{t,c}$ were tested, and for each case, a characteristic curve was generated by systematically varying $p_{out}/p_{t,c}$.

The sensitivity analysis results, depicted in Figure 10, reveal that both the bypass ratio and pressure loss coefficient exhibit significant dependence on $T_{t,b}/T_{t,c}$, demonstrating that the temperature ratio independence assumption is not valid for these performance parameters. Two alternative parameters, also depicted in Figure 10, show negligible $T_{t,b}/T_{t,c}$ sensitivity, while adequately representing flow regulation and total pressure losses. The first one is the corrected bypass mass flow rate ($\dot{m}_{corr,b}$). The second is the relative momentum difference between the inlet and outlet, calculated as in Equation (1). The momentum $\mathcal{M}$ is defined with Equation (2) that applied to a one-dimensional flow aligned with the

Downloaded from https://www.cambridge.org/core. 17 Nov 2026 at 02:24:13, subject to the Cambridge Core terms of use.

Table 6. *Test matrix used for validation of map independence from absolute thermodynamic state*

Parameter	Value(s)
$p_{t,c}$ (kPa)	264
$p_{t,b}/p_{t,c}$	0.94, 1.02, 1.10
$p_{out}/p_{t,c}$	0.86 to 0.98
$T_{t,c}$ (K)	870
$T_{t,b}/T_{t,c}$	0.3983
A_b/A_c	0.335

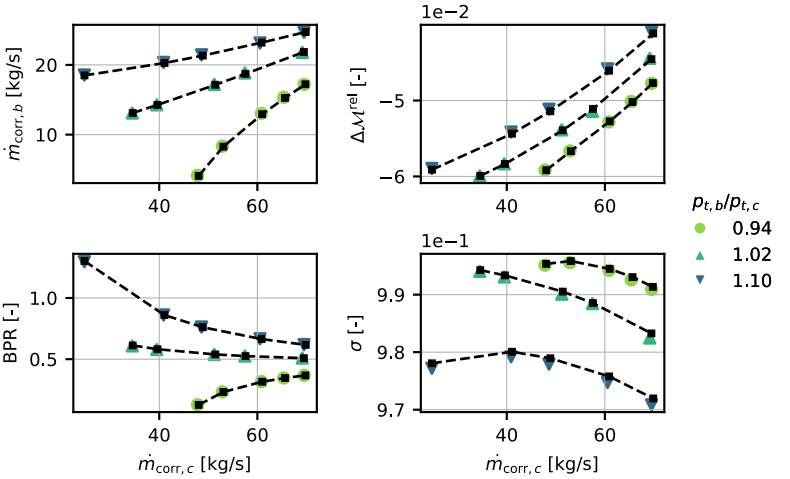


Figure 11. *Verification of map independence from the absolute thermodynamic state through comparison with CFD simulations at identical non-dimensional inputs and different absolute pressure levels. Performed at* $A_b/A_c = 0.335$.

axial direction, and considering the inlet and outlet of the VABI, develops in:

$$\mathcal{M}_{in} = v_c\,\dot{m}_c + v_b\,\dot{m}_b + A_c\,p_c + A_b\,p_b \tag{9}$$

$$\mathcal{M}_{out} = v_{out}\,\dot{m}_{out} + A_{out}\,p_{out} \tag{10}$$

To verify that the component behaviour depends only on non-dimensional parameters and not on absolute thermodynamic state, additional CFD simulations were performed at some selected map operating points. These simulations use different absolute inlet total pressures than those used to create the original map, while maintaining identical non-dimensional input parameters. A summary of the values used for these simulations is shown in Table 6. Figure 11 presents a comparison between the original performance map data (coloured scattered points) and the validation simulation results (black points connected by dashed lines).

The close match between the tested points and the map curves confirms that the proposed parameter reduction is effective, with performance independent of the absolute thermodynamic state within the investigated range. Therefore, it can be applied as long as the non-dimensional input parameters lie within the map bounds. The complete rear-VABI performance map, expressed in terms of the selected input and output parameters, is presented in Figure 12. The performance characteristics are expressed in terms of $\dot{m}_{corr,b}$ and $\Delta\mathcal{M}^{rel}$. The latter is shown in percentage. The performance map shows that increasing A_b/A_c moves the operation toward higher corrected bypass mass flow rates. The relative momentum

Downloaded from https://www.cambridge.org/core. 17 Nov 2026 at 02:24:13, subject to the Cambridge Core terms of use.

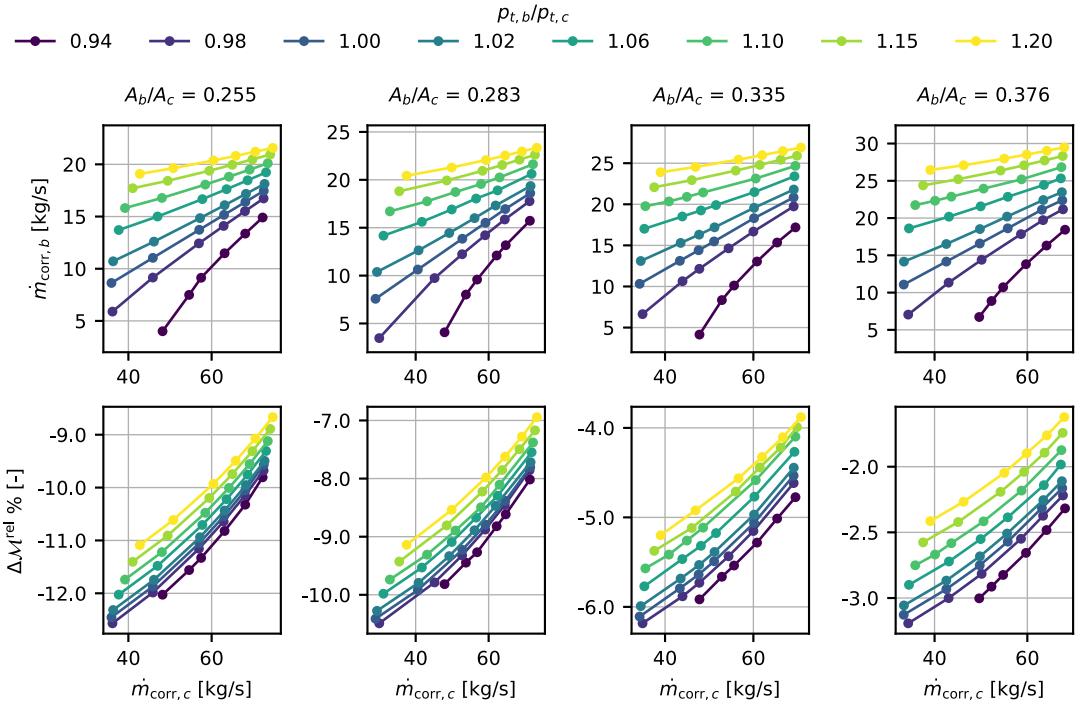


Figure 12. *Full performance map of the VABI.*

difference is defined as the normalised difference between inlet and outlet momentum. Its negative values indicate a net momentum gain from inlet to outlet, which arises because the sum of A_b and A_c does not equal A_{out} due to the presence of the area regulator and the plug. The momentum gain due to area change consistently exceeds friction losses, keeping $\Delta\mathcal{M}^{rel}$ negative throughout the map. Three trends can be observed in the momentum loss distribution shown in the map. First, at fixed area ratio, $\Delta\mathcal{M}^{rel}$ increases in magnitude with increasing mass flow rate: higher corrected mass flow rates result from lower back pressure, which raises flow velocities and pressure losses, while the area-induced momentum gain remains constant. Second, increasing total pressure ratio at fixed area ratio leads to higher momentum losses. Third, higher area ratios produce higher momentum loss. This is attributed to the increased bypass mass flow entering the system at higher A_b/A_c, which intensifies core-bypass mixing and the associated losses, outweighing the reduction in area-induced momentum gain from the larger inlet area.

4.0 Demonstration of the VABI in a three-stream engine

In this section, the results of the CFD simulations are used to create a reduced-order VABI model in Modelon Impact. This model is used in a notional three-stream VCE to study the effect of the VABI area regulator position on the engine performance and flow-holding capabilities.

4.1 Practical implementation in Modelon Impact

The performance maps extracted from the CFD simulations are used to construct a VABI model in Modelon Impact [24], which is built on the Modelica language [25], an acausal, equation-based, object-oriented programming language designed for physical system modelling. Unlike causal languages, Modelica represents physical systems as sets of differential-algebraic equations (DAEs) without pre-defined input–output causality. Once a model is constructed, Modelon Impact compiles it using the

Downloaded from https://www.cambridge.org/core. 17 Nov 2026 at 02:24:13, subject to the Cambridge Core terms of use.

Optimica Compiler Toolkit (OCT) [26], which symbolically processes the Modelica equations, performs index reduction for DAEs and generates an executable representation in the form of a Functional Mock-up Unit (FMU) [27]. For steady-state analysis, the problem reduces to solving a nonlinear algebraic system:

$$\mathbf{R}(\mathbf{x}) = \mathbf{0} \tag{11}$$

where $\mathbf{x}$ denotes the vector of iteration variables (IVs), and $\mathbf{R}(\mathbf{x})$ represents the residual equations derived from component matching and system constraints. In the context of gas turbine modelling, typical IVs include spool speeds (N_L, N_H) and turbomachinery matching parameters such as R-lines. The residual equations enforce conditions such as shaft torque balance, mass-flow compatibility and thermodynamic closure. The nonlinear system is solved using a solver based on Krylov Inexact Newton SOLver (KINSOL), part of the SUite of Nonlinear and DIfferential/ALgebraic equation Solvers (SUNDIALS) suite [28]. The solver implements a Newton-based method with advanced features, such as line search, damping strategies and preconditioned iterative linear solvers, to improve robustness and convergence. At each iteration, the solver updates IVs by approximately solving:

$$\mathbf{x}^{(k+1)} = \mathbf{x}^{(k)} - \mathbf{J}^{-1}(\mathbf{x}^{(k)})\,\mathbf{R}(\mathbf{x}^{(k)}) \tag{12}$$

where $\mathbf{J} = \frac{\partial \mathbf{R}}{\partial \mathbf{x}}$ is the Jacobian of residuals with respect to IVs. Convergence is achieved when the residual norm falls below a specified tolerance, ensuring all matching conditions are satisfied simultaneously.

For jet engine simulations, mixer component calculations involve two phases: on-design and off-design. In the on-design phase, all engine design parameters, such as compressor pressure ratios, bypass ratio and mass flow ratio, are freely specified by the designer and imposed on the engine components. With these imposed parameters, each component is sized, which includes both the physical sizing of flow areas and the scaling of performance maps. For a conventional mixer component, this involves sizing inlet areas to meet a specific design Mach number, typically that of the core flow at the mixing plane. This procedure introduces three IVs: core area, bypass area and total exit pressure. These IVs are solved against residual equations enforcing core Mach number, static pressure balance at the mixing plane and momentum balance over the mixer, respectively. In the off-design phase, the inlet areas are fixed, with the IVs changing to bypass mass flow rate and total exit pressure, with residuals enforcing static pressure and momentum balance.

For the VABI developed in this work, the procedure differs. The residual equations derived from static pressure and momentum balance in a constant-area duct are replaced by residuals based on performance map continuity. Three maps are considered:

- Relative momentum difference map
- Bypass corrected mass flow map
- Core corrected mass flow map

Each map uses the same three input parameters: β, $p_{\mathrm{t,b}}/p_{\mathrm{t,c}}$ and $A_{\mathrm{b}}/A_{\mathrm{c}}$. Ideally, $\dot{m}_{\mathrm{corr},c}$ would be used directly as an input, but trilinear interpolation requires a rectilinear grid in the input space, which is not achievable for $\dot{m}_{\mathrm{corr},c}$, given the CFD sampling strategy. Consequently, an artificial parameter β is introduced, varying from 0 to 1 in fixed steps. This β becomes an IV, iterated until the desired $\dot{m}_{\mathrm{corr},c}$ is achieved, forming a first IV-residual pair.

The second IV–residual pair consists of the outlet total pressure, which is varied until the following momentum balance equation is satisfied:

$$\left(1 - \Delta\mathcal{M}^{\mathrm{rel}}\right)\left[(\dot{m}v + pA)_c + (\dot{m}v + pA)_b\right] = (\dot{m}v + pA)_e \tag{13}$$

For the third pair, the on- and off-design behaviour is different. For on-design, the complete state for the inlets, including $p_{\mathrm{t,b}}/p_{\mathrm{t,c}}$ and $\dot{m}_{\mathrm{corr},b}$, is defined by the engine design parameters. As β is already used for the matching of $\dot{m}_{\mathrm{corr},c}$, that only leaves the map input parameter $A_{\mathrm{b}}/A_{\mathrm{c}}$ available to be used as IV. The $A_{\mathrm{b}}/A_{\mathrm{c}}$ that solves the $\dot{m}_{\mathrm{corr},b}$ continuity equation will be defined as the design area ratio, forming the default area regulator position. In off-design, $\dot{m}_{\mathrm{corr},b}$ is no longer imposed, but will result from the

Downloaded from https://www.cambridge.org/core. 17 Nov 2026 at 02:24:13, subject to the Cambridge Core terms of use.

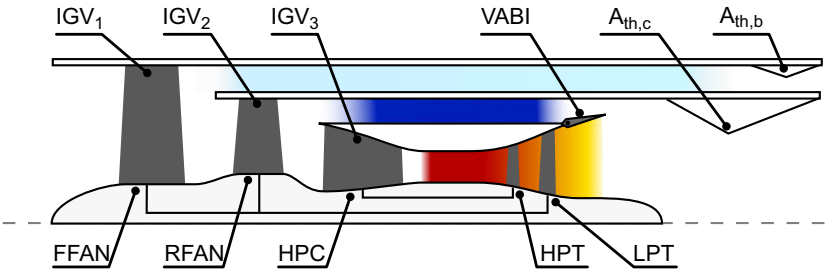


Figure 13. *Three-stream VCE used to demonstrate the VABI components in a system model.*

Table 7. *Engine design parameters*

Parameter	Value	Unit
T_4	1600	K
$\dot{m}_{air}$	95	kg/s
OPR	30	–
PR_{FFAN}	2.15	–
PR_{RFAN}	2.33	–
BPR_{outer}	0.08	–
BPR_{inner}	0.40	–

Table 8. *Engine technology limits*

Parameter	Value	Unit
$\eta_{p,FFAN}$	90	%
$\eta_{p,RFAN}$	90	%
$\eta_{p,HPC}$	90	%
$\eta_{p,HPT}$	85	%
$\eta_{p,LPT}$	85	%
Nozzle thrust coefficient	1	–
Inlet pressure recovery	1	–

off-design matching of the turbomachinery. This adds one degree of freedom, which allows to impose A_b/A_c as a control parameter. As such, the residual equation of $\dot{m}_{corr,\,b}$ continuity will be solved by an IV outside of the VABI component from an engine system level.

4.2 Simulation results in a notional three-stream VCE

The VABI model is demonstrated in a notional three-stream VCE architecture. A schematic representation of the VCE is shown in Figure 13. The configuration consists of a core stream, a mixed bypass stream (inner bypass) and an unmixed bypass stream (outer bypass). In the three-stream VCE, the VABI controls the inner bypass ratio.

The engine design parameters and technology levels are summarised in Tables 7 and 8. These were selected such that the VABI map fits the engine without requiring scaling of corrected air flows or cross-sectional areas in the map. The design point is set at a flight Mach number of 0.8 and an altitude of 10 km. A VCE of this type can include various variable geometries, such as nozzles, inlet guide vanes (IGVs), VABIs and nozzle guide vanes (NGVs) [29]. However, for this demonstration, only the VABI is implemented.

Downloaded from https://www.cambridge.org/core. 17 Nov 2026 at 02:24:13, subject to the Cambridge Core terms of use.

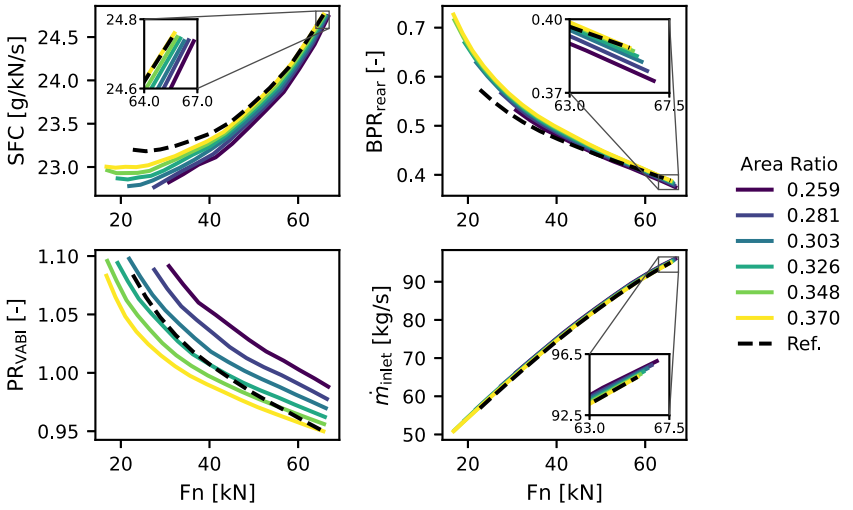


Figure 14. *Several performance indicators for the VCE as a function of thrust output and VABI position, indicated as area ratio at the mixing plane. The reference engine performance is indicated with the dashed line.*

Two engine models are produced:

- **Reference engine:** Implements the conventional static-pressure-balance VABI.
- **Map-driven VABI engine:** Implements the VABI using performance maps derived from CFD data.

After completing the on-design simulations, a series of throttle curves are generated for both engines under on-design flight conditions by performing a sweep on turbine inlet temperature (T_4) between 900 K and 1, 600 K. For the map-driven VABI engine, multiple curves are produced that correspond to VABI positions ranging from fully closed to fully open. These positions correspond to area ratios of 0.259 and 0.370, respectively, with the latter coinciding with the design VABI position. For the reference engine, only the design VABI position is used, as the regulation would maintain a constant total mixing-plane area, invalidating a direct comparison.

Figure 14 summarises the results, showing specific fuel consumption (SFC), $\mathrm{BPR}_{\mathrm{rear}}$, $\mathrm{PR}_{\mathrm{VABI}}$ and inlet mass flow rate ($\dot{m}_{\mathrm{inlet}}$) as functions of uninstalled thrust output (F_n). The VABI pressure ratio is defined as:

$$\mathrm{PR}_{\mathrm{VABI}} = \frac{p_{\mathrm{t,b}}}{p_{\mathrm{t,c}}}.$$

The rear bypass ratio increases sharply when the throttle is reduced for all curves, including the reference engine. The VABI position influences $\mathrm{BPR}_{\mathrm{rear}}$ as expected: more closed positions reduce the bypass ratio. However, the variation within the studied VABI positions is limited to 3.5% at maximum throttle, with differences becoming larger at lower throttle settings. The reference engine exhibits distinctly different behaviour compared to the map-driven VABI engine, confirming once more that the static pressure balance assumption is not valid for the considered VABI geometry.

All cases show an increase of $\mathrm{PR}_{\mathrm{VABI}}$ as the throttle is reduced. Across all curves, $\mathrm{PR}_{\mathrm{VABI}}$ approaches 1.1, after which the engine model fails to converge. $\mathrm{PR}_{\mathrm{VABI}}$ and $\mathrm{BPR}_{\mathrm{rear}}$ are inversely related: as $\mathrm{BPR}_{\mathrm{rear}}$ decreases, the RFAN processes less air, reducing its power consumption. This surplus power is used to increase compression, raising $\mathrm{PR}_{\mathrm{VABI}}$. Again, the reference engine shows different behaviour, reinforcing that the static pressure balance assumption is invalid.

Downloaded from https://www.cambridge.org/core. 17 Nov 2026 at 02:24:13, subject to the Cambridge Core terms of use.

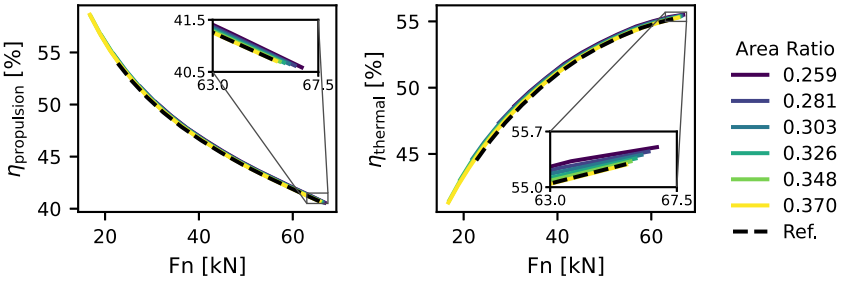


Figure 15. *Propulsive and thermal efficiency of the VCE using the VABI map. The static-pressure-balance engine reference is shown as the dashed line.*

One advantage often cited for VCE engines is their flow-holding capability, where intake mass flow remains high at low throttle to reduce installation losses [30–32]. However, Figure 14 shows only a modest variation of the inlet mass flow rate ($\approx 1.0\%$) as the VABI area ratio changes. Other variable geometries, such as changes in nozzle throat area, have been shown in the literature to have a much larger effect [12, 33]. In this instance, the design area ratio corresponds to the most open position, and as such, only a closing is possible. Counterintuitively, closing the area regulator actually increases the mass flow rate through the engine. This is because the total pressure upstream of the core nozzle increases, which can force more airflow through the choked nozzle. The effect is small, however, as it is counterbalanced by a slight increase in total temperature, resulting from a decrease in BPR.

The SFC curves indicate that the efficiency bucket occurs at relatively low thrust (≈ 20 kN). When the VABI closes, the PR_{VABI} limit is often reached before this region. Nevertheless, closing the VABI improves the SFC under the given flight conditions. This is explained by Figure 15, which shows propulsion and thermal efficiency defined as:

$$\eta_{\text{thermal}} = \frac{\dot{m}_{\text{n,c}} v_{\text{n,c}}^2 + \dot{m}_{\text{n,b}} v_{\text{n,b}}^2 - \dot{m}_{\text{amb}} v_{\text{amb}}^2}{2\dot{q}} \tag{14}$$

$$\eta_{\text{propulsion}} = 2v_{\text{amb}} \cdot \frac{\dot{m}_{\text{n,c}} v_{\text{n,c}} + \dot{m}_{\text{n,b}} v_{\text{n,b}} - \dot{m}_{\text{amb}} v_{\text{amb}}}{\dot{m}_{\text{n,c}} v_{\text{n,c}}^2 + \dot{m}_{\text{n,b}} v_{\text{n,b}}^2 - \dot{m}_{\text{amb}} v_{\text{amb}}^2} \tag{15}$$

with the subscripts "n, b", "n, c" and "amb" referring to bypass nozzle exit, core nozzle exit, and ambient flight conditions, respectively.

Both efficiencies improve slightly when closing the VABI. Thermal efficiency increases with higher Overall Pressure Ratio (OPR). Closing the VABI increases nozzle exit velocities, thereby raising the propulsion efficiency and thrust. Combined with the downward slope of the propulsion efficiency curve, throttle curves for more closed VABI positions come out slightly ahead of more open ones. Lastly, the reference engine again shows a different SFC behaviour compared to the map-driven VABI engine.

5.0 Conclusion

This paper presented a methodology for generating a reduced-order model of a VABI based on high-fidelity numerical simulations and integrating it into system-level propulsion simulations. The approach establishes relationships between three non-dimensional input parameters and two key outputs: the corrected bypass mass flow rate and a loss metric derived from the relative momentum difference between the inlets and outlet.

From the high-fidelity analysis, two important findings emerge. First, the commonly used pressure loss coefficient exhibits a significant dependency on the inlet temperature ratio $T_{t,b}/T_{t,c}$, which is often neglected in the literature. Secondly, the corrected bypass mass flow rate $\dot{m}_{\text{corr},b}$ and the relative momentum difference $\Delta\mathcal{M}^{\text{rel}}$ show negligible sensitivity to the temperature ratio when the

Downloaded from https://www.cambridge.org/core. 17 Nov 2026 at 02:24:13, subject to the Cambridge Core terms of use.

other non-dimensional parameters are kept fixed, making them more representative for wider system simulations.

The assumption of static pressure balance at the mixing plane, widely adopted in conventional 0-D mixer models, was shown to be a strong simplification that deviates from the actual fluid-dynamic behaviour. An alternative methodology employing the VABI performance map was proposed and implemented in a notional three-stream variable-cycle engine. A comparison with a conventional mixer model revealed significant differences in off-design performance, indicating that the static-pressure balance assumption is inadequate for practical mixer geometries. Furthermore, the VABI demonstrated its ability to produce modest changes in engine bypass ratio (up to 4%), thereby influencing the throttle curves shape and specific fuel consumption (up to 1.3% at partial throttle).

Overall, the proposed methodology enables accurate integration of reduced-order VABI components into propulsion system simulations while reducing reliance on oversimplified assumptions, thereby improving fidelity in off-design performance prediction.

Acknowledgments. Funded by the European Union. Views and opinions expressed are, however, those of the authors only and do not necessarily reflect those of the European Union or the European Commission. Neither the European Union nor the granting authority can be held responsible for them. The authors would also like to thank the Modelon support received from Jim Claesson, head of Physics Engineering at Modelon AB and the support from professor Svend Bram at the Vrije Universiteit Brussel for proofreading the manuscript.

References

[1] Grazzini, G., Milazzo, A. and Mazzelli, F. *Ejectors for Efficient Refrigeration: Design, Applications and Computational Fluid Dynamics*, Springer, 2018, Cham.
[2] Besagni, G. Ejectors on the cutting edge: the past, the present and the perspective, *Energy*, 2019, **170**, pp 998–1003.
[3] Hunter, C., Presz, W. and Reynolds, G. Thrust augmentation with mixer/ejector system, in *th AIAA Aerospace Sciences Meeting & Exhibit*. American Institute of Aeronautics and Astronautics, 2002, Reno,NV, USA.
[4] Aidoun, Z., et al. Current advances in ejector modeling, experimentation and applications for refrigeration and heat pumps. Part 1: single-phase ejectors, *Inventions*, 2019, **4**, pp 15.
[5] Rayee, T., Verstraete, D. and Hendrick, P. Development of a mixer model to compare mixed and unmixed HBPR turbofans, in *th AIAA/ASME/SAE/ASEE Joint Propulsion Conference & Exhibit*, American Institute of Aeronautics and Astronautics, 2008, Hartford, CT.
[6] Fejer, A.A., et al. Research on mixing of coaxial streams, in *Report AD0654014*, Illinois Institute of Technology, 1967, Chicago, IL.
[7] Hu, H., et al. Mixing process in a lobed jet flow, *AIAA J.*, 2002, **40**, pp 1339–1345.
[8] Cooper, N., Merati, P. and Hu, H. Numerical simulation of the vortical structures in a lobed jet mixing flow, in *43rd AIAA Aerospace Sciences Meeting and Exhibit*, American Institute of Aeronautics and Astronautics, 2005, Reno, Nevada.
[9] Kurzke, J. and Halliwell, I. *Propulsion and Power*, Springer International Publishing, 2018, Cham.
[10] Van Den Berghe, J., et al. A. 1D model for the unsteady gas dynamics of ejectors, *Energy*, 2023, **267**, pp 126551.
[11] Van Den Berghe, J., Mendez, M.A. and Bartosiewicz, Y. An extension of the compound flow theory with friction between the streams and at the wall, *J. Fluid Mech.*, 2024, **1000**, pp A85, arXiv: 2401.07236 [physics].
[12] Van Den Borre, K. and Saracoglu, B. Optimization of variable cycle engine throttle schedules using gradient-free methods, *J. Eng. Gas Turb. Power*, **2025**, pp 1–24.
[13] Van Den Borre, K., Bruno, G.M. and Saracoglu, B.H.Quantitative comparison of two variable cycle engine concepts, in *AIAA SciTech 2026 Forum.*, American Institute of Aeronautics and Astronautics, 2026, Orlando, FL.
[14] Liu, R., et al. Numerical study of steady flow characteristics of a rear variable-area bypass injector with alternating area regulator, *Chin. J. Aeronaut.*, 2024, **37**, pp 180–198.
[15] Dandani, M., et al. Numerical study of mixing enhancement in 2D supersonic ejector, *Int. J. Turb. Jet Eng.*, 2022, **39**, pp 501–511.
[16] Koutmos, P. and McGuirk, J.J. CFD predictions of lobed mixer performance, *Comput. Method Appl. Mech. Eng.*,1995, **122**, pp 131–144.
[17] Huang, G., et al. Investigations of entrainment characteristics and shear-layer vortices evolution in an axisymmetric rear variable area bypass injector, *Chin. J. Aeronaut.*, 2022, **35**, pp 230–244.
[18] Cooper, N., Merati, P. and Hu, H. Numerical simulation of the vortical structures in a lobed jet mixing flow, in *43rd AIAA Aerospace Sciences Meeting and Exhibit*, American Institute of Aeronautics and Astronautics, 2005, Reno, Nevada.
[19] Salman, H., Page, G.J. and McGuirk, J.J. Prediction of lobed mixer vortical structures with a k - e turbulence model, *AIAA J.*, 2003, **41**, pp 878–887.
[20] Van den Borre, K., Saracoglu, B.H. and Coussement, A. Numerical modelling of hydrogen combustion phenomena in a dual-mode Ramjet engine with cavity flameho, in *AIAA SciTech 2023 Forum*, American Institute of Aeronautics and Astronautics, 2023, National Harbor, MD & Online.

Downloaded from https://www.cambridge.org/core. 17 Nov 2026 at 02:24:13, subject to the Cambridge Core terms of use.

[21] Zore, K., et al. ANSYS scale resolving simulations of launch-vehicle configuration at transonic speeds, in *th Annual CFD Symposium*, 2019, pp 8–9.
[22] Xu, Z., et al. A multi-fidelity simulation method research on front variable area byp ass injector of an adaptive cycle engine, *Chin. J. Aeronaut.*, 2022, **35**, pp 202–219.
[23] Song, F., et al. Integration of high-fidelity model of forward variable area bypass injector into zero-dimensional variable cycle engine model, *Chin. J. Aeronaut.*, 2021, **34**, pp 1–15.
[24] Modelon Impact Webpage. 2025. https://modelon.com/modelon-impact/
[25] Modelica AssociationModelica - A Unified Object-Oriented Language for Systems Modeling - Language Specification, 2017. https://modelica.org/documents/ModelicaSpec34.pdf
[26] Modelon, A.B. *OPTIMICA Compiler Toolkit User Manual*, 2023.
[27] FMI Standard. 2025. https://fmi-standard.org
[28] Hindmarsh, A.C., et al. SUNDIALS: suite of nonlinear and differential/algebraic equation solvers, In *ACM Transactions on Mathematical Software 31.3*, 2005, pp 363–396.
[29] Johnson, J.E. Variable cycle engine developments at general electric -1955-1995, in *Developments In High-Speed Vehicle Propulsion Systems*, 1996, pp 105–158.
[30] Clark, R.A., Tai, J.C. and Mavris, D.N. Development of a parametric variable cycle engine model using the multiple design point approach, in *AIAA SciTech 2023 Forum.* American Institute of Aeronautics and Astronautics, 2023, National Harbor, MD, USA.
[31] Denney, R.K., et al. Variable cycle optimization for supersonic commercial applications, in *Aerospace Technology Conference and Exposition*, 2005, pp 2005-01-3400.
[32] Zenkner, S., et al. Variable cycle engine concepts and component technologies—An overview, *J. Eng. Gas Turb. Power*, 2025, **147**, pp 051004.
[33] Chen, M., Zhang, J. and Tang, H. Performance analysis of a three-stream adaptive cycle engine during throttling, *Int. J. Aerosp. Eng.*, 2018, **2018**, pp 1–16.

Cite this article: Ponti M., Van den Borre K., Bruno G. M. and Saracoglu B. H. Numerical analysis and reduced-order modelling of a variable area mixer. *The Aeronautical Journal*, https://doi.org/10.1017/aer.2026.10231

Downloaded from https://www.cambridge.org/core. 17 Nov 2026 at 02:24:13, subject to the Cambridge Core terms of use.